Magnetic resonance imaging is more sensitive than PET for detecting treatment-induced cell death-dependent changes in glycolysis

Richard L. Hesketh[1], Jiazheng Wang[1], Alan J. Wright[1], David Y. Lewis[1,3], Alice E. Denton[4], Richard Grenfell[1], Jodi L. Miller[1], Robert Bielik[1], Marcel Gehrung[1], Maria Fala[1], Susana Ros[1], Bangwen Xie[1], De-en Hu[1], Kevin M. Brindle[1,2].

1. CRUK Cambridge Institute, University of Cambridge, Li Ka Shing Centre, Robinson Way, Cambridge, CB2 0RE.
2. Department of Biochemistry, University of Cambridge, Tennis Court Road, Cambridge, CB2 1QW.
3. CRUK Beatson Institute, Switchback Road, Bearsden, Glasgow, G61 1BD.
4. Lymphocyte Signalling and Development, Babraham Hall House, Babraham Cambridge, CB22 3AT.

Running Title: Hyperpolarized MR and PET imaging of tumor cell death.

Keywords: Hyperpolarized [1-^{13}C]pyruvate, FDG-PET, tumor, cell death, treatment response.

Abbreviations:

[^{18}F]FDG, 2-([^{18}F]fluoro)-2-deoxy-D-glucose; [^{18}F]FDG-6-*P,* 2-([^{18}F]fluoro)-2-deoxy-D-glucose-6-phosphate; [^{18}F]FDG-1,6-P_2, 2-([^{18}F]fluoro)-2-deoxy-D-glucose-1,6-bisphosphate; [^{18}F]FD-PGL, 2-([^{18}F]fluoro)-2-deoxy-6-phospho-D-gluconolactone; CC3, cleaved caspase-3; FACS, fluorescence activated cell sorting; GAPDH, glyceraldehyde-3-phosphate dehydrogenase; GLUT, glucose transporter; HK, hexokinase; LDH, lactate dehydrogenase; MCT, monocarboxylate transporter; MRI, magnetic resonance imaging; PARP, poly-ADP ribose polymerase; PK, pyruvate kinase; TCA cycle, tricarboxcylic acid cycle; TRAIL, tumor necrosis factor-related apoptosis inducing ligand; TUNEL, terminal deoxynucleotidyl transferase nick-end labeling.

Financial support: The work was supported by a Cancer Research UK Programme grant (17242) and by the CRUK-EPSRC Imaging Centre in Cambridge and Manchester (16465) awarded to K. M. Brindle.

Declaration of competing financial interests:
The hyperpolarizer is on loan from GE Healthcare (GEH) and is the subject of a research agreement between the University of Cambridge, Cancer Research UK and GE Healthcare. KMB holds patents with GEH on some aspects of DNP technology.

Corresponding author: Prof. Kevin M. Brindle, Cancer Research UK Cambridge Institute, Li Ka Shing Centre, Robinson Way, Cambridge, CB2 0RE, United Kingdom, Phone: 01223 769647; Fax: 01223 766002; e-mail: kmb1001@cam.ac.uk

Abstract

Metabolic imaging has been widely used to measure the early responses of tumors to treatment. Here we assess the abilities of positron emission tomography (PET) measurement of [^{18}F]FDG uptake and magnetic resonance imaging (MRI) measurement of hyperpolarized [1-^{13}C]pyruvate metabolism to detect early changes in glycolysis following treatment-induced cell death in human colorectal (Colo205) and breast adenocarcinoma (MDA-MB-231) xenografts in mice. A TRAIL agonist that binds to human but not mouse cells induced tumor-selective cell death. Tumor glycolysis was assessed by injecting [1,6-$^{13}C_2$]glucose and measuring ^{13}C-labeled metabolites in tumor extracts. Injection of hyperpolarized [1-^{13}C]pyruvate induced rapid reduction in lactate labeling. This decrease, which correlated with an increase in histological markers of cell death and preceded decrease in tumor volume, reflected reduced flux from glucose to lactate and decreased lactate concentration. However, [^{18}F]FDG uptake and phosphorylation was maintained following treatment, which has been attributed previously to increased [^{18}F]FDG uptake by infiltrating immune cells. Quantification of [^{18}F]FDG uptake in flow-sorted tumor and immune cells from disaggregated tumors identified CD11b+/CD45+ macrophages as the most [^{18}F]FDG-avid cell type present, yet they represented <5% of the cells present in the tumors and could not explain the failure of [^{18}F]FDG-PET to detect treatment response. MRI measurement of hyperpolarized [1-^{13}C]pyruvate metabolism is therefore a more sensitive marker of the early decreases in glycolytic flux that occur following cell death than PET measurements of [^{18}F]FDG uptake.

Statement of Significance

Findings demonstrate superior sensitivity of MRI measurement of hyperpolarized [1-^{13}C]pyruvate metabolism versus PET measurement of ^{18}F-FDG uptake for detecting early changes in glycolysis following treatment-induced tumor cell death.

Introduction

Tumors are increasingly categorized according to their biology (1) and a new generation of drugs are being developed that target the mutated pathways often found in tumors (2). Treatment response is typically assessed using morphological imaging (computed tomography (CT) or magnetic resonance imaging (MRI) (3)) with response being categorized according to guidelines such as the Response Evaluation Criteria of Solid Tumors (RECIST) (4). However, changes in size are often slow to manifest after treatment (5-7). To complement the advances in therapy, new imaging techniques are required that can accurately assess early treatment responses. These could facilitate switching non-responders to a more effective treatment, limit unnecessary side effects and costs of an ineffective therapy, and speed up clinical translation of new treatments.

Biochemical changes can occur before volumetric changes and therefore targeted metabolic imaging could improve the timescale of response detection (8). Positron emission tomography (PET) using the glucose analogue, 2-([^{18}F]fluoro)-2-deoxy-D-glucose ([^{18}F]FDG) has been used to assess treatment response, notably in lymphomas (9,10). However, concerns about the “flare” effect, a poorly understood phenomenon of increased tracer uptake soon after treatment attributed to agonistic effects of therapy on macrophage infiltration and activation, have often led to delayed [^{18}F]FDG-PET imaging of treatment response (11-14).

^{13}C magnetic resonance spectroscopic imaging (MRSI) of hyperpolarized [1-^{13}C]pyruvate metabolism has been shown to give an early indication of tumor treatment response (15,16). However, for hyperpolarized [1-^{13}C]pyruvate to enter routine clinical practice, it must demonstrate that it can provide information not available from [^{18}F]FDG studies. In this study we used a multivalent TRAIL agonist

(MEDI3039) targeting the human death receptor five (DR5) to activate the extrinsic pathway of apoptosis in xenograft models of human colorectal and breast cancer (17) and compared the ability of hyperpolarized [1-^{13}C]pyruvate and [^{18}F]FDG-PET to detect early response to treatment *in vivo*. A reduction in label flux between hyperpolarized [1-^{13}C]pyruvate and the endogenous lactate pool preceded changes in tumor volume and reliably detected treatment response whereas PET measurements of [^{18}F]FDG uptake largely failed to detect response.

Materials and Methods

Cell culture

Colo205 human colon adenocarcinoma cells (ATCC, VA, USA) and MDA-MB-231 triple-negative breast adenocarcinoma cells (ATCC) were transduced with a lentiviral vector expressing mStrawberry red fluorescent protein and luciferase (18). Colo205 cells were cultured in RPMI medium (Life Technologies, CA, USA), supplemented with 2 mM L-glutamine and 10% heat-inactivated fetal bovine serum (Life Technologies). MDA-MB-231 cells were cultured in DMEM (Life Technologies) supplemented with 10% FBS. Both cell lines tested negative for mycoplasma and were used within ten passages from the original stocks.

Animal preparation

Animal experiments were performed in compliance with a project licence issued under the Animals (Scientific Procedures) Act of 1986. Protocols were approved by the Cancer Research UK, Cambridge Institute Animal Welfare and Ethical Review Body.

Colo205 or MDA-MB-231 cells (5×10^6) were resuspended in 0.2 mL PBS or a 50:50 mix of Matrigel (Corning, NY, USA) and complete DMEM, respectively, and implanted subcutaneously in the flanks of female BALB/c *nu/nu* mice (Charles River, Wilmington, MA). Tumors were imaged when they reached ~0.8 cm^3. For imaging mice were fasted for 6 – 8 h (19) and kept in a warmed chamber (32ºC) for 1 h prior to induction of anesthesia using 1 – 2.5 % isoflurane (Isoflo, Abbotts Laboratories Ltd, Maidenhead, UK) in a 50:50 mix of air (1 L/min) and oxygen (1 L/min). MEDI3039, a TRAIL agonist, (Medimmune, Cambridge, UK) was administered intravenously (i.v.) at 0.4 mg/kg (17,20).

Hyperpolarization of [1-^{13}C]pyruvate

A 44 mg sample of [1-^{13}C]pyruvic acid (Cambridge Isotope Laboratories, Tewkesbury, MA, USA) containing 15 mM of OX063 trityl radical (GE Healthcare, Amersham, UK) and 1.5 mM of gadoterate meglumine (Dotarem, Guerbet, Roissy, France) was hyperpolarized at ~ 1.2 K by microwave irradiation at 94.110 GHz and 100 mW in a 3.35 T Hypersense polarizer (Oxford Instruments, Abingdon, UK) for approximately 1 h (21). The frozen sample was rapidly dissolved in 6 mL buffer containing 40 mM HEPES, 94 mM NaOH, 30 mM NaCl and 100 mg/L EDTA heated to 180 ºC and pressurized to 10 bar to yield a final [1-^{13}C]pyruvate concentration of approximately 75 mM.

Imaging Treatment Response

Colo205 (n=18, Table S1) and MDA-MB231 (n=22, Table S2) tumor-bearing mice underwent bioluminescence (BLI), fluorescence (FLI), MR and PET-CT imaging performed in the same 2 h sessions before and 24 h after treatment with MEDI3039

(Figure S1). FLI and BLI were performed using a Xenogen IVIS 200 (Perkin Elmer, MA, USA). Fluorescence images of mStrawberry expression were acquired using a DSRed filter (λ_{ex}=500-550 nm, λ_{em}=575-650 nm) and corrected for background autofluorescence. Bioluminescence images were acquired 5 min after intraperitoneal injection of 150 mg/kg of 15 mg/ml D-luciferin. Regions of interest (ROIs) were analyzed using Living Image v4.5 software (Perkin Elmer).

After BLI, 12.9±1.8 MBq [^{18}F]FDG (in approximately 100 µL) (Alliance Medical, Guildford, UK) was injected i.v.. MRI was performed in a 7.0 T horizontal bore magnet (Agilent, Palo Alto, CA) using an actively decoupled dual-tuned ^{13}C/^{1}H volume transmit coil (Rapid Biomedical, Rimpar, Germany) and a 20 mm diameter ^{13}C receiver coil (Rapid Biomedical). For anatomical reference eight axial T_2-weighted ^{1}H images were acquired using a fast-spin echo sequence with a slice thickness of 2.5 mm, field-of-view 40 × 40 mm and matrix size of 256 × 256 points. ^{13}C images were acquired using spectral spatial (SpSp) pulses and a 3D dual-spin echo (DSE) acquisition (22). Flip angles were 7º for [1-^{13}C]pyruvate and 45º for [1-^{13}C]lactate. Five [1-^{13}C]pyruvate images were acquired prior to the first [1-^{13}C]lactate image, after which each metabolite was excited with a temporal resolution of 2 s per metabolite. Injection of hyperpolarized [1-^{13}C]pyruvate, which can cause transient hypoxia, was delayed for 1 h post-[^{18}F]FDG injection to minimise any effects on [^{18}F]FDG uptake (23). Hyperpolarized [1-^{13}C]pyruvate (15 mL/kg) was injected i.v. over 8 s and the pulse sequence was started 2 s after the start of infusion. Images were acquired over 90 s and analyzed in Matlab (Mathworks, MA, USA). A 3D tumor ROI was defined on the T_2-weighted image and the rate of hyperpolarized ^{13}C label exchange was assessed by measuring the ratio of the areas under the pyruvate and lactate labeling curves (AUC). This ratio is related directly to the apparent first order

rate constant describing label exchange between the injected pyruvate and the endogenous lactate pool (24).

A 15 min static PET acquisition began at 90 min post-injection of [^{18}F]FDG using a nanoScan PET/CT (Mediso, Budapest, Hungary). A helical CT was acquired for anatomical reference and attenuation correction. PET images, with a nominal isotropic resolution of 0.3 mm, were reconstructed using a 3D ordered-subset expectation maximization (OSEM) method in one to three coincidence modes, eight iterations and six subsets. Images were normalized and corrected for decay, dead-time, random events and attenuation. The images were analyzed using Vivoquant 3.0 software (InviCRO, Massachusetts, USA). A 3D tumor ROI was drawn manually and Otsu thresholding applied to better delineate the tumor. Mean and maximum standardized uptake values (SUV) were calculated using:

$$SUV = \frac{c_{img}}{ID/BW}$$

where c_{img} is the activity concentration (MBq/mL) derived from the image ROI, ID is the injected dose and BW is the body weight of the animal.

Dynamic [^{18}F]FDG-PET

Three h PET scans were acquired in a separate cohort of Colo205 tumor-bearing mice (n=9) following injection of 8.12 ± 1.13 MBq [^{18}F]FDG before and 24 h after treatment with MEDI3039. Scans were reconstructed with a nominal isotropic resolution of 0.6 mm using a 3D OSEM method with one to five coincidence modes, two iterations and six subsets, with CT acquisition and PET corrections applied as for static image acquisitions. Scans were reconstructed into 50 time frames (5 s × 12, 0–1 min; 2 min × 30, 0–60 min; 15 min × 8, 60–180 min). A 3D ROI drawn manually over the inferior vena cava between the level of the kidneys and diaphragm was

thresholded at 75% of the maximum activity and used as an image-derived input function. A 3D tumor ROI was Otsu thresholded on the 165 – 180 min dataset. Patlak analysis was used to estimate the net influx rate of [^{18}F]FDG (k_i) from the linear portion of the graph between 20 and 60 min (25). The mean r^2 for linear regression fitting was 0.97±0.03.

Dynamic contrast enhanced MRI

A separate cohort of Colo205 tumor-bearing mice (n=3 per group, drug- and vehicle-treated) underwent dynamic contrast-enhanced (DCE)-MRI before and 24 h after treatment with MEDI3039. Baseline spin-lattice relaxation rates ($R_{1,pre}=1/T_1$) were measured using an inversion recovery fast low angle shot (FLASH) sequence (TR 5.5 ms, TE 2.5 ms, 10 s delay between acquisitions, 2 averages per inversion time). To obtain a pre-contrast R_1 map these data were fitted voxel-by-voxel to a mono-exponential function:

$$S = S_0[1 - 2\, e^{-T_I/T_1}]$$

where T_I is the inversion time. A T_1-weighted gradient-echo pulse sequence was used with 4×1.5 mm thick axial slices with 0.25 mm gaps covering the tumor region, field-of-view 40×40 mm, data matrix 128×128, TR 110 ms, TE 9 ms. Ten baseline images were collected prior to the injection, over 8 s, of 200 μmoles/kg i.v. Dotarem (Guerbet). Forty images were acquired immediately after injection and a further nine timepoints generated from averaging blocks of nine images acquired every 10 min up to 90 min post-injection. Images were converted to R_1 relaxation rate maps using:

$$S = S_0 \frac{(1- e^{-TR/T_1})\sin\theta}{1- e^{-TR/T_1}\cos\theta}$$

where S_0 is the relaxed signal (TR >> T_1) and θ is the flip angle used in the gradient-echo sequence (27º). Changes in R_1 were directly converted to gadolinium (Gd^{3+}) concentration curves as described in (26).

Whole-body [^{18}F]FDG autoradiography and mStrawberry fluorescence imaging

A separate cohort of Colo205 tumor-bearing mice (n=3 per group, drug- and vehicle-treated) were injected i.v. with [^{18}F]FDG, culled after 90 min and immediately frozen by submersion in liquid nitrogen-cooled isopentane. Axial cryo-sections (10 µm thick) were thaw-mounted onto glass slides (CM3050S Cryostat, Leica, Wetzlar, Germany). The slides were apposed to a storage phosphor screen (GE Healthcare) overnight to produce autoradiographs with a pixel size of 10 µm using a Typhoon Biomolecular Imager (Amersham). Red fluorescence images of the cryo-sections were acquired using a 532 nm laser, long-pass 550 nm filter and a pixel size of 10 µm. The slides were subsequently H&E stained and fluorescence, autoradiography and H&E images were co-registered manually.

Determining the cellular fate of [^{18}F]FDG using fluorescence-activated cell sorting

A separate cohort of Colo205 tumor-bearing mice (n=3 per group, drug- and vehicle-treated) were injected i.v. with 140±4.9 MBq [^{18}F]FDG and after 90 min the tumors excised and single cell suspensions were prepared by digestion in 1 mg/mL collagenase I (Sigma-Aldrich, MO, USA) and 0.1 mg/mL DNase I (Roche, Penzburg, Germany) at 37ºC for 45 min with trituration at 15 min intervals. The cells were washed in PBS/2 mM EDTA and labeled by incubation with anti-CD45 (30-F11), anti-CD11b (M1/70) (Biolegend, CA, USA) and live/dead fixable viability dye e780

(ThermoFisher Scientific, MA, USA) at 4ºC for 1 h. CD11b+/CD45+ phagocytes, CD45-/mStrawberry+ tumor cells, CD45-/mStrawberry- non-hematopoetic, non-tumor cells and e780+ dead cells were sorted on a BD Influx flow sorter (BD Biosciences, NJ, USA). Flow cytometric data were analyzed using FlowJo V10.0 (FlowJo LLC, OR, USA). The radioactivity (cpm) of each cell population was determined using a well-counter (Nuklear-Medizintechnik, Dresden, Germany) and converted to Bq using a calibration curve.

[1,6-$^{13}C_2$]glucose infusion and ^{13}C and ^{1}H NMR spectroscopy of tumor extracts

A separate cohort of Colo205 tumor-bearing mice (n=3 per group, drug- and vehicle-treated) were infused with [1,6-$^{13}C_2$]glucose as described previously (27). Tumors were freeze-clamped and blood obtained by cardiac puncture. Tissue extracts were prepared by addition of 5 µL/mg 2 M perchloric acid (PCA) and homogenization in a Precellys 24 homogenizer (Stretton Scientific, Stretton, UK). Extracts were pH corrected to 7.0, lyophilized and dissolved in deuterium oxide. Two µmoles trimethylsilylpropanoic acid (TMSP) were added as a chemical shift standard (0 p.p.m.). High-resolution ^{1}H and ^{1}H-decoupled ^{13}C NMR spectra were acquired at 294 K using a 5 mm probe and a 600 MHz NMR spectrometer (Bruker, MA, USA). The acquisition conditions for ^{13}C spectroscopy were 30º flip angle, 15000 transients, spectral width 36.8 kHz, acquisition time 1.8 s and a relaxation delay 1.2 s. The acquisition conditions for ^{1}H spectroscopy were 90º flip angle, 1024 transients, spectral width 10 kHz, acquisition time 3.3 s, relaxation delay 2 s. Data were phased and baseline corrected and peak integrals calculated using Topspin 4.0 (Bruker).

Analysis of [^{18}F]FDG and radiolabeled metabolites in tumor extracts

A separate cohort of Colo205 tumor-bearing mice (n=3 per group, drug- and vehicle-treated) were anesthetized and injected i.v. with 146.2±7.8 MBq [^{18}F]FDG (~200 µL). After 90 min tumors were excised and homogenized in ice-cold 4 M PCA using a Precellys 24 homogenizer (Stretton Scientific, Stretton, UK). The extracts were neutralized with 8 M KOH and passed through a 0.2 µm syringe filter (Whatman, Maidstone, UK). Radio-high performance liquid chromatography (radioHPLC) was performed using a Dionex UltiMate 3000 HPLC system (ThermoFisher Scientific) (28). Samples (100 µL) were injected into the system, separated using a Partasil SAX 10 µm column (250 mm × 4.6 mm, Sigma-Aldrich) and eluted with a linear gradient of 300 mM sodium dihydrogen phosphate containing 2% methanol (A) and 2% methanol in water (B). The gradient profile was 0–15 min 5% A, 15–25 min 50% A (isocratic), with a flow rate of 1.5 ml/min. Radioactivity was detected using a fLumo HPLC NaI detector (Berthold Technologies, Bad Wildbad, Germany) connected to the column outflow. Metabolite retention times for [^{18}F]FDG and [^{18}F]FDG-6-*P* were assigned using standards, while 2-([^{18}F]fluoro)-2-deoxy-6-phospho-D-gluconolactone ([^{18}F]FD-PGL) and 2-([^{18}F]fluoro)-2-deoxy-D-glucose-1,6-bisphosphate ([^{18}F]FDG-1,6-P_2) were assigned using data from (28).

Western blotting

Freeze-clamped tumor samples (n=7 per group, drug- and vehicle-treated) were homogenized in 10 µL/mg modified RIPA buffer (50 mM HEPES, 1 mM EDTA, 0.7% sodium deoxycholate, 1% Nonidet P-40, 0.5 M lithium chloride, pH 7.6, 1 cOmplete mini EDTA-free protease inhibitor (Sigma-Aldrich) using a Precellys 24

homogenizer. Proteins were separated by SDS-PAGE and transferred to a nitrocellulose membrane (iBlot 2, Thermofisher Scientific). Membranes were blocked with 1:1 Odyssey blocking buffer and TBS and incubated with antibody solutions (Table S3) at 4ºC overnight. Antibodies were detected using multiplexed IRDye secondary antibodies and images acquired using an Odyssey CLx (LI-COR Biosciences, NE, USA).

Enzyme activity and ATP assays

Lactate dehydrogenase (LDH) activity was determined spectrophotometrically in tumor extracts (n=7 per group, drug- and vehicle-treated) prepared in RIPA buffer (29). Colorimetric kits were used to determine glyceraldehyde 3-phosphate dehydrogenase (GAPDH) activity (ab204732, Abcam, Cambridge, UK) and ATP concentration (ab83355, Abcam), while a fluorometric kit was used to determine pyruvate kinase (PK) activity (ab83432, Abcam). A PHERAstar FS microplate reader (BMG Labtech, Aylesbury, UK) was used for all spectrophotometric measurements.

Immunohistochemistry

Sections of formalin-fixed paraffin-embedded tumors were stained for cleaved caspase-3 (CC3) and terminal deoxynucleotidyl transferase nick-end labeling (TUNEL) (20). Percentage positivity for each stain was calculated using positive pixel count algorithms in Aperio ImageScope 12.3.3 (Leica).

Analysis

Statistical and graphical analysis was performed using Prism v6.0 (GraphPad, CA, USA). Statistical tests performed were paired or unpaired *t*-tests with errors

representing standard deviation, unless stated otherwise. *P* values are summarized in figures as: <0.0001, ****; 0.0001 – 0.001, ***; 0.001 – 0.01, ** and 0.01 to 0.05, *.

Results

MEDI3039 induces cell death and tumor regression

Colo205 tumor-bearing mice (n=3) were treated with 0.4 mg/kg MEDI3039 i.v. weekly for four weeks and fortnightly thereafter (a total of fourteen doses over six months). There was a decrease in tumor volume from 0.95 ± 0.1 cm^3 to 0.03 ± 0.02 cm^3 12 days after initial treatment, after which tumor volumes decreased to below the detection limit on T_2-weighted MRI (Fig. 1a-d). Bioluminescence and red fluorescence intensity decreased over the first month, after which one tumor started to regrow while the other two continued to decrease in intensity (Fig. 1e-l). At six months the tumor that regrew had reached its size limit while in the other two mice the tumors remained undetectable.

Histological and reporter gene evaluation of early response to therapy

Colo205 and MDA-MB-231 tumor-bearing mice underwent combined BLI, FLI, [1-^{13}C]pyruvate-magnetic resonance imaging (MRI) and [^{18}F]FDG-PET imaging before and 24 h after treatment with MEDI3039 (Colo205, n=10; MDA-MB-231, n=12) or drug vehicle (saline) (Colo205 n=8; MDA-MB-231, n=9) (Tables 1, S1 & S2). CC3 staining increased from 21.8±11.6% to 58.51±14.4% (*P* = 0.0002, n=7 per group, drug- and vehicle-treated) in Colo205 tumors (Fig. 2 a-c) and from 19±5.1% to 57.7±19.3% (*P* =0.006, n=5 drug-treated and n=4 vehicle-treated) in MDA-MB-231 tumors (Fig. 2 d-f). TUNEL staining increased from 8.0±6.7% to 19.4±6.3% (*P*=0.007, n=7 per group, drug- and vehicle-treated) in Colo205 tumors (Fig. 2 g-i) and 6.6±2.0%

to 21.1±6.1% (*P*=0.003, n=5 drug-treated and n=4 vehicle-treated) in MDA-MB-231 tumors (Fig. 2 j-l). There was no significant decrease in tumor volumes after 24 h (Fig. S2 a-f). mStrawberry fluorescence decreased in MDA-MB-231 tumors by 45.3±28.6% (*P*=0.0002, n=12), but there was no change in Colo205 tumors (*P*=0.30, n=8). However, fluorescence in Colo205 tumors had decreased by 48 h after treatment (*P*=0.04; n=3). With the exception of one animal, tumor bioluminescence decreased after treatment, with 57.3±53.3% (*P*=0.0053; n=10) and 68.5±24.8% (*P*=<0.0001; n=12) decreases in Colo205 and MDA-MB-231 tumors, respectively. Measurements of ATP concentration in Colo205 tumor extracts showed a decrease from 0.36±0.1 to 0.14±0.05 μmol/g w.w. (*P*=0.0008; n=11) at 24 h after treatment.

Imaging early response to MEDI3039 treatment using ^{13}C MRI and PET

3D ^{13}C MRS images showed a post-treatment decrease of the [1-^{13}C]lactate/[1-^{13}C]pyruvate ratio (the ratio of the areas under the lactate and pyruvate labeling curves) in all animals, with a mean reduction of 42.2±15.9% (*P*=0.004; n=7) and 36.3±18.6% (*P*=0.007; n=7) in Colo205 (Fig. 3 a-c) and MDA-MB-231 (Fig. 3 d-e) tumors, respectively (Table 1). There was no change in [^{18}F]FDG-PET SUV_{max} (2.1±0.3 to 2.1±0.4, *P*=0.82, n=7) or SUV_{mean} (1.1±0.2 to 1.1±0.2 , *P*=0.6, n=7) in Colo205 tumors. In MDA-MB-231 tumors SUV_{max} did not change significantly (2.2±0.4 to 2.0±0.3, *P*=0.2, n=10), but there was a decrease in SUV_{mean} (1.0±0.2 to 0.9±0.2; *P*=0.048, n=10). However, this was a decrease of 14±21%, compared to a 36±19% decrease in [1-^{13}C]lactate/[1-^{13}C]pyruvate ratio, indicating that changes in [1-^{13}C]pyruvate metabolism were more sensitive for detecting response to treatment in these tumors.

Confirmation that [^{18}F]FDG-PET fails to detect response to MEDI3039

[^{18}F]FDG tumor/muscle ratios derived from autoradiography (Fig. S3 a-g) and mean percentage injected dose per gram (%ID/g) from well-counting of excised Colo205 tumors (Fig. S3 h) also did not change significantly following treatment (Table 1). However, in a separate cohort of Colo205 tumor-bearing mice (n=9), MEDI3039 treatment resulted in the net [^{18}F]FDG influx rate (k_i) decreasing from 0.048±0.01 to 0.037±0.012 min^{-1} (P=0.051).

Colo205 tumor-bearing mice (n=3) were further imaged 24, 48 and 72 h after MEDI3039 treatment. Mean SUV_{max} showed no significant change, with a value of 1.67±0.1 before treatment and 1.79±0.5 (P=0.77) 72 h after treatment, despite significant decreases in tumor volume.

DCE-MRI showed an increase in perfusion after MEDI3039 treatment

In a separate cohort of Colo205 tumor-bearing mice (n=3) treatment response was assessed using DCE-MRI (Fig. S4). Tumor gadolinium (Gd^{3+}) concentration increased in all mice after treatment from 0.05±0.009 to 0.09±0.02 mM at 10 min post-injection although the small sample size meant this was not statistically significant. The rate of contrast agent clearance was similar in pre-treatment and post-treatment tumors.

Determination of the cellular fate of [^{18}F]FDG using fluorescence-activated cell sorting of disaggregated tumors

Tumor cells (mStrawberry+, CD45-) comprised 78.3±5.2% of the sorted cells in untreated tumors (n=3) (Fig. 4 a,c) and 71.6 ± 9.4% in MEDI3039-treated tumors

(n=3) (Fig. 4 b,c) at 24 h after treatment (P = 0.3). Phagocytes (CD45+, CD11b+) comprised 1.6±0.4% of cells in untreated tumors and 2.3±1.7% after treatment (P = 0.5) (Fig 4 a-c). Treatment resulted in a decrease in tumor cell [^{18}F]FDG uptake (%ID/cell) from $2.1\times10^{-9}\pm5.0\times10^{-10}$% to $7.5\times10^{-10}\pm2.7\times10^{-10}$% ($P$=0.01). Phagocytes were the most [^{18}F]FDG avid cell-type, taking up approximately 5× the uptake of tumor cells (Fig. 4d). Treatment also decreased [^{18}F]FDG uptake per phagocyte, from $1.2\times10^{-8}\pm2.5\times10^{-9}$% to $6.5\times10^{-9}\pm1.9\times10^{-9}$ (P=0.04). Due to there being approximately 50× and 30× more tumor cells than phagocytes in untreated and treated tumors, respectively, the contribution of phagocytes to [^{18}F]FDG uptake in the tumor as a whole remained small despite their greater [^{18}F]FDG uptake per cell. Correction for % cell type, represented as %ID per million total cells, showed that in untreated tumors uptake in the tumor cell population was $2\times10^{-3}\pm5\times10^{-4}$% per million total cells in the tumor, whereas in phagocytes it was $2\times10^{-4}\pm8.7\times10^{-5}$% per million total cells. After treatment uptake in the tumor cell population was $6\times10^{-4}\pm5.5\times10^{-4}$%, whereas in the phagocyte population it was $1\times10^{-4}\pm5.6\times10^{-5}$% (Fig. 4e).

MEDI3039-induced changes in the expression of enzymes and transporters involved in [^{18}F]FDG and [1-^{13}C]pyruvate metabolism in Colo205 tumors

Treatment decreased the expression of MCT1 and to a lesser extent MCT4 (P=0.005 and P=0.02, respectively, n=7) (Fig. 5 a-b). LDH activity and expression were unchanged, (P=0.07 and P=0.9, respectively, n=7) (Table S4, Fig. 5 c,h). Expression of GLUT1 and GLUT3 decreased (P=0.01 and P=0.0001, respectively, n=7) (Fig. 5 d-e), while HK2 expression was unchanged (P=0.1, n=7) (Fig. 5f). PARP cleavage by caspase-3, a feature of apoptosis, increased significantly after

MEDI3039 treatment (*P*=0.005, n=7) (Fig. 5g). There were no significant changes in the activities of GAPDH (Fig. 5i) or PK (Fig. 5j).

Measurement of glycolytic flux in MEDI3039-treated Colo205 tumors using [1,6-$^{13}C_2$]glucose

Colo205 tumor-bearing mice (n=3 per group, drug- and vehicle-treated) were infused with [1,6-$^{13}C_2$]glucose for 150 min. ^{13}C enrichment of blood glucose was 50.0±7.2% and was unaffected by treatment. The expected tumor metabolite labelling patterns are shown in Fig. 6 c. There was a decrease in tumor [3-^{13}C]lactate concentration from 1259±297 μmoles/g w.w. to 363±148 μmoles/g w.w. 24 h after treatment (*P*=0.01) (Fig. 6 a,b,d), a decrease in [3-^{13}C]alanine concentration, from 233±59 to 37.6±19 μmoles/g w.w. (*P*=0.03) and a decrease in TCA cycle metabolite and [4-^{13}C]glutamate labelling (Fig. 6 a-b). There was no significant change in [1,6-$^{13}C_2$]glucose concentration in the tumors, which decreased from 425±169 to 279±135 μmoles/g w.w. (*P*=0.3).

Measurement of [^{18}F]FDG and its metabolites in tumor extracts

HPLC peaks at 2 and 6 min corresponded to [^{18}F]FDG and [^{18}F]FDG-6-*P*, respectively (Fig. S5 a-b). The ratio of [^{18}F]FDG/[^{18}F]FDG-6-*P* was 6.2±3% in untreated tumors and 7.0±3.7% after treatment (n=3 per group, drug- and vehicle-treated, *P*=0.8) (Fig. S5 c). HPLC peaks were also observed at 8.5, 9, 20 and 22.5 min. The peak at 20 min, assigned to [^{18}F]FD-6-PGL (28), was decreased in treated tumors suggesting that MEDI3039 treatment reduced flux into the pentose phosphate pathway.

Discussion

Imaging with hyperpolarized [1-^{13}C]pyruvate has the potential to be used clinically to detect early tumor responses to treatment (15,30). Pre-clinical studies in breast cancer and glioma models demonstrated reductions in label flux from [1-^{13}C]pyruvate to lactate prior to a reduction in tumor volume (31,32), while in other studies hyperpolarized [1-^{13}C]pyruvate was no more sensitive than measurements of tumor volume or [^{18}F]FDG uptake in detecting treatment response (33-35).

Drug treatment can have direct effects on metabolic pathways, for example, etoposide can inhibit oxidative phosphorylation (36,37) and PI3K inhibitors can decrease LDH expression (38). Therefore, any effects observed with metabolic imaging may be drug-specific, rather than a generic measure of treatment response (36). Here we used a targeted agent to induce apoptosis that avoided potential direct effects of the drug on glycolytic enzyme expression. This allowed study of the specific effects that cell death has on the tumor metabolism of hyperpolarized [1-^{13}C]pyruvate and [^{18}F]FDG. Engineering the tumor cells to express mStrawberry and luciferase gave independent markers that could be used to confirm treatment response *in vivo*. Although MEDI3039 activates the extrinsic pathway of apoptosis other mechanisms of cell death, particularly secondary necrosis, undoubtedly co-exist following treatment and are not discriminated between in these experiments (39).

Survival increased from under two weeks in control animals to a minimum of six months in treated mice and there was complete response in two out of three tumors. Treatment-induced cell death was demonstrated histologically by marked

increases in CC3 and TUNEL staining at 24 h, and functionally by a decrease in mStrawberry fluorescence at 24 h and 48 h in MDA-MB-231 and Colo205 tumors, respectively. The delayed decrease in Colo205 tumors was attributed to delayed clearance of the mStrawberry protein, possibly indicating a higher proportion of macrophage uptake and apoptotic as compared to necrotic cell death (40). Cell death resulted in a decrease in ATP concentration in both tumor types and consequent reduction in bioluminescence. In both tumor types label flux from hyperpolarized [1-^{13}C]pyruvate to lactate was decreased and this preceded changes in tumor volume.

Exchange of hyperpolarized ^{13}C label between pyruvate and lactate depends on tumor perfusion, MCT and LDH expression and lactate pool size. Since DCE-MRI measurements showed a small increase in tumor perfusion and there was no change in LDH expression the decrease in exchange must have been due to the large decrease in lactate pool size, which through the accompanying decrease in NADH concentration will decrease LDH activity, and by decreased MCT1 and MCT4 transporter expression, which will decrease pyruvate transport (41,42). We have shown previously, albeit in another tumor cell type, that LDH and the MCTs have comparable flux control coefficients for the exchange and that the exchange is linearly dependent on lactate concentration (41,42). Given the large decrease in lactate concentration and more modest decrease in MCT expression it seems likely that the decreased exchange is largely the result of the decrease in lactate concentration, resulting from a decrease in glycolytic flux, and consequent decrease in LDH activity. Furthermore, we observed significant PARP cleavage, which has previously been correlated with depletion of the NAD(H) pool and consequent decrease of LDH activity (33,34).

The lack of a significant decrease in [^{18}F]FDG uptake in treated tumors was surprising given the degree of cell death observed histologically. [^{18}F]FDG accumulation in tissues is multi-factorial, with no consistent relationship between [^{18}F]FDG uptake and GLUT and hexokinase expression (43,44). In dynamic PET measurements [^{18}F]FDG uptake remained irreversible 3 h after injection demonstrating that glucose-6-phosphatase activity, previously implicated in the failure of response detection with [^{18}F]FDG-PET, was minimal in these tumors (45). Although we observed significant decreases in GLUT1 and GLUT3 expression, HK2 expression did not change. Therefore, in these tumors HK2 activity appears to dominate [^{18}F]FDG trapping, which would explain the persistence of [^{18}F]FDG uptake following treatment. Although the levels of ATP were decreased in the tumor these were evidently sufficient to maintain [^{18}F]FDG phosphorylation. In Colo205 tumors, the trend towards a decrease in net [^{18}F]FDG influx rate (k_i) after treatment indicates that a kinetic analysis may detect changes that are not apparent from the SUV. However, the hyperpolarized [1-^{13}C]pyruvate/[1-^{13}C]lactate ratio, in which pyruvate delivery is accounted for, may be a more practical clinical approach than kinetic analysis of [^{18}F]FDG uptake, which requires prolonged dynamic image acquisition and arterial blood sampling.

^{13}C NMR measurements of [1,6-$^{13}C_2$]glucose metabolism and radioHPLC measurements of [^{18}F]FDG metabolism showed that treatment of Colo205 tumors reduced glycolytic flux to lactate and flux into the TCA cycle but that phosphorylation of [^{18}F]FDG was maintained. This suggests that, contrary to the generally accepted view, [^{18}F]FDG-6-*P* accumulation in tumors is not necessarily reflective of glycolytic flux and that the differential response seen with [^{18}F]FDG-PET and [1-^{13}C]pyruvate is not due to a switch to oxidative metabolism after treatment. That hyperpolarized [1-

^{13}C]pyruvate can detect changes in glycolytic flux, but not [^{18}F]FDG, is a reflection of the fact that the rate of exchange between pyruvate and lactate is partly dependent on the lactate concentration, which is determined primarily by glycolytic flux, whereas the accumulation of [^{18}F]FDG is only dependent on transport and phosphorylation (41).

The failure of [^{18}F]FDG to detect treatment response has frequently been attributed to activation of phagocytic cells and, to a lesser extent other immune cells, resulting in a paradoxical increase in tumor [^{18}F]FDG uptake (12,14,46,47). Here [^{18}F]FDG uptake per cell was quantified by sorting labeled cell populations using FACS. We defined a phagocytic population as CD45+/CD11b+, presumed to be mostly macrophages (48). The majority of this population was also positive for mStrawberry+, both before and after treatment, indicating tumor cell phagocytosis. Although macrophages were the most glycolytically active cell type, their low numbers meant that the majority of [^{18}F]FDG] in the tumor accumulated in tumor cells. Using micro-autoradiography Kubota et al. reported that high [^{18}F]FDG uptake corresponded to areas infiltrated with macrophages, which is frequently cited as the basis of the metabolic flare effect (49). Although our findings corroborate this previous work, we show that while macrophages are the most [^{18}F]FDG-avid cell-type, they represent such a small component of the tumors that their overall contribution to [^{18}F]FDG uptake is relatively insignificant. This excludes inflammatory cell infiltration as a cause of the failure of [^{18}F]FDG to detect treatment response in this study.

The general implications of our findings are limited by the use subcutaneous human xenografts in immuno-compromised mice, which have greatly reduced numbers of T-cells. However, the proportion of macrophages in Colo205 tumors was

similar to the proportion reported in most early human colorectal tumors (<5%) (50). In tumors with a greater degree of immune cell infiltration [^{18}F]FDG uptake may have a more significant impact on [^{18}F]FDG-PET results. A further limitation of the experiments performed to elicit mechanisms responsible for changes in [^{18}F]FDG and [1-^{13}C]pyruvate metabolism was the small cohort sizes in some experiments (n=3 in each group for several of the experiments). Nevertheless, the majority of results were statistically significant.

Conclusion

We have shown that hyperpolarized [1-^{13}C]pyruvate can be used to detect treatment-induced tumor cell death, with decreases in lactate labeling preceding a reduction in tumor volume, whereas there was no significant change in [^{18}F]FDG or glucose uptake, despite a large decrease in glycolytic flux. Tumor [^{18}F]FDG-6-*P* accumulation was not significantly affected by inflammatory cell infiltration.

Acknowledgements

We would like to thank Matt Clayton, Mike Mitchell and Ryan Asby for their help with animal experiments and Jane Gray and Ian Hall for their expertise in Western blotting and *ex-vivo* fluorescence imaging. We would also like to thank the members of the PET-CT department at Addenbrookes' Hospital for their generous provision of [^{18}F]FDG.

References

1. Cancer Genome Atlas N. Comprehensive molecular characterization of human colon and rectal cancer. Nature **2012**;487:330-7
2. Garraway LA. Genomics-driven oncology: framework for an emerging paradigm. J Clin Oncol **2013**;31:1806-14

3. Tirkes T, Hollar MA, Tann M, Kohli MD, Akisik F, Sandrasegaran K. Response criteria in oncologic imaging: review of traditional and new criteria. Radiographics **2013**;33:1323-41
4. Eisenhauer EA, Therasse P, Bogaerts J, Schwartz LH, Sargent D, Ford R*, et al.* New response evaluation criteria in solid tumours: revised RECIST guideline (version 1.1). Eur J Cancer **2009**;45:228-47
5. Katz SI, Hammer M, Bagley SJ, Aggarwal C, Bauml JM, Thompson JC*, et al.* Radiologic Pseudoprogression during Anti-PD-1 Therapy for Advanced Non-Small Cell Lung Cancer. J Thorac Oncol **2018**;13:978-86
6. Neves AA, Brindle KM. Assessing responses to cancer therapy using molecular imaging. Biochim Biophys Acta **2006**;1766:242-61
7. Dimitrakopoulou-Strauss A, Ronellenfitsch U, Cheng C, Pan L, Sachpekidis C, Hohenberger P*, et al.* Imaging therapy response of gastrointestinal stromal tumors (GIST) with FDG PET, CT and MRI: a systematic review. Clin Transl Imaging **2017**;5:183-97
8. Brindle K. New approaches for imaging tumour responses to treatment. Nat Rev Cancer **2008**;8:94-107
9. Biggi A, Gallamini A, Chauvie S, Hutchings M, Kostakoglu L, Gregianin M*, et al.* International validation study for interim PET in ABVD-treated, advanced-stage hodgkin lymphoma: interpretation criteria and concordance rate among reviewers. J Nucl Med **2013**;54:683-90
10. Borchmann P, Goergen H, Kobe C, Lohri A, Greil R, Eichenauer DA*, et al.* PET-guided treatment in patients with advanced-stage Hodgkin's lymphoma (HD18): final results of an open-label, international, randomised phase 3 trial by the German Hodgkin Study Group. Lancet **2018**;390:2790-802
11. Wolchok JD, Hoos A, O'Day S, Weber JS, Hamid O, Lebbe C*, et al.* Guidelines for the evaluation of immune therapy activity in solid tumors: immune-related response criteria. Clin Cancer Res **2009**;15:7412-20
12. Findlay M, Young H, Cunningham D, Iveson A, Cronin B, Hickish T*, et al.* Noninvasive monitoring of tumor metabolism using fluorodeoxyglucose and positron emission tomography in colorectal cancer liver metastases: correlation with tumor response to fluorouracil. J Clin Oncol **1996**;14:700-8
13. Skoura E, Ardeshna K, Halsey R, Wan S, Kayani I. False-Positive 18F-FDG PET/CT Imaging: Dramatic "Flare Response" After Rituximab Administration. Clin Nucl Med **2016**;41:e171-2
14. Mortimer JE, Dehdashti F, Siegel BA, Trinkaus K, Katzenellenbogen JA, Welch MJ. Metabolic flare: indicator of hormone responsiveness in advanced breast cancer. J Clin Oncol **2001**;19:2797-803
15. Aggarwal R, Vigneron DB, Kurhanewicz J. Hyperpolarized 1-[13C]-Pyruvate Magnetic Resonance Imaging Detects an Early Metabolic Response to Androgen Ablation Therapy in Prostate Cancer. Eur Urol **2017**;72:1028-9
16. Hesketh RL, Brindle KM. Magnetic resonance imaging of cancer metabolism with hyperpolarized (13)C-labeled cell metabolites. Curr Opin Chem Biol **2018**;45:187-94
17. Greer Y, Gilbert S, Tice D, Lipkowitz S. Abstract 3494: MEDI3039, a novel highly potent tumor necrosis factor (TNF)-related apoptosis-inducing ligand (TRAIL) receptor agonist, induces apoptotic cell death in breast cancer cells. Cancer Research **2016**;76:3494-

18. Patrick PS, Hammersley J, Loizou L, Kettunen MI, Rodrigues TB, Hu DE*, et al.* Dual-modality gene reporter for in vivo imaging. Proc Natl Acad Sci U S A **2014**;111:415-20
19. Serrao EM, Rodrigues TB, Gallagher FA, Kettunen MI, Kennedy BW, Vowler SL*, et al.* Effects of fasting on serial measurements of hyperpolarized [1-(13) C]pyruvate metabolism in tumors. NMR Biomed **2016**;29:1048-55
20. Xie B, Tomaszewski MR, Neves AA, Ros S, Hu DE, McGuire S*, et al.* Optoacoustic Detection of Early Therapy-Induced Tumor Cell Death Using a Targeted Imaging Agent. Clin Cancer Res **2017**;23:6893-903
21. Ardenkjaer-Larsen JH, Fridlund B, Gram A, Hansson G, Hansson L, Lerche MH*, et al.* Increase in signal-to-noise ratio of > 10,000 times in liquid-state NMR. Proc Natl Acad Sci U S A **2003**;100:10158-63
22. Wang J, Wright AJ, Hu DE, Hesketh R, Brindle KM. Single shot three-dimensional pulse sequence for hyperpolarized (13) C MRI. Magn Reson Med **2017**;77:740-52
23. Takakusagi Y, Matsumoto S, Saito K, Matsuo M, Kishimoto S, Wojtkowiak JW*, et al.* Pyruvate induces transient tumor hypoxia by enhancing mitochondrial oxygen consumption and potentiates the anti-tumor effect of a hypoxia-activated prodrug TH-302. PLoS One **2014**;9:e107995
24. Hill DK, Orton MR, Mariotti E, Boult JK, Panek R, Jafar M*, et al.* Model free approach to kinetic analysis of real-time hyperpolarized 13C magnetic resonance spectroscopy data. PLoS One **2013**;8:e71996
25. Patlak CS, Blasberg RG, Fenstermacher JD. Graphical evaluation of blood-to-brain transfer constants from multiple-time uptake data. J Cereb Blood Flow Metab **1983**;3:1-7
26. Noebauer-Huhmann IM, Szomolanyi P, Juras V, Kraff O, Ladd ME, Trattnig S. Gadolinium-based magnetic resonance contrast agents at 7 Tesla: in vitro T1 relaxivities in human blood plasma. Invest Radiol **2010**;45:554-8
27. Marin-Valencia I, Yang C, Mashimo T, Cho S, Baek H, Yang XL*, et al.* Analysis of tumor metabolism reveals mitochondrial glucose oxidation in genetically diverse human glioblastomas in the mouse brain in vivo. Cell Metab **2012**;15:827-37
28. Rokka J, Gronroos TJ, Viljanen T, Solin O, Haaparanta-Solin M. HPLC and TLC methods for analysis of [(18)F]FDG and its metabolites from biological samples. J Chromatogr B Analyt Technol Biomed Life Sci **2017**;1048:140-9
29. Bergmeyer H, Bernt E. Lactate Dehydrogenase. In: Bergmeyer HU, editor. Methods of Enzymatic Analysis (Second Edition): Academic Press; 1974. p 574.
30. Nelson SJ, Kurhanewicz J, Vigneron DB, Larson PE, Harzstark AL, Ferrone M*, et al.* Metabolic imaging of patients with prostate cancer using hyperpolarized [1-(1)(3)C]pyruvate. Sci Transl Med **2013**;5:198ra08
31. Witney TH, Kettunen MI, Hu DE, Gallagher FA, Bohndiek SE, Napolitano R*, et al.* Detecting treatment response in a model of human breast adenocarcinoma using hyperpolarised [1-13C]pyruvate and [1,4-13C2]fumarate. Br J Cancer **2010**;103:1400-6
32. Day SE, Kettunen MI, Cherukuri MK, Mitchell JB, Lizak MJ, Morris HD*, et al.* Detecting response of rat C6 glioma tumors to radiotherapy using hyperpolarized [1- 13C]pyruvate and 13C magnetic resonance spectroscopic imaging. Magn Reson Med **2011**;65:557-63

33. Witney TH, Kettunen MI, Day SE, Hu DE, Neves AA, Gallagher FA*, et al.* A comparison between radiolabeled fluorodeoxyglucose uptake and hyperpolarized (13)C-labeled pyruvate utilization as methods for detecting tumor response to treatment. Neoplasia **2009**;11:574-82, 1 p following 82
34. Day SE, Kettunen MI, Gallagher FA, Hu DE, Lerche M, Wolber J*, et al.* Detecting tumor response to treatment using hyperpolarized 13C magnetic resonance imaging and spectroscopy. Nat Med **2007**;13:1382-7
35. Ravoori MK, Singh SP, Lee J, Bankson JA, Kundra V. In Vivo Assessment of Ovarian Tumor Response to Tyrosine Kinase Inhibitor Pazopanib by Using Hyperpolarized 13C-Pyruvate MR Spectroscopy and 18F-FDG PET/CT Imaging in a Mouse Model. Radiology **2017**;285:830-8
36. Demel HR, Feuerecker B, Piontek G, Seidl C, Blechert B, Pickhard A*, et al.* Effects of topoisomerase inhibitors that induce DNA damage response on glucose metabolism and PI3K/Akt/mTOR signaling in multiple myeloma cells. Am J Cancer Res **2015**;5:1649-64
37. Yadav N, Kumar S, Marlowe T, Chaudhary AK, Kumar R, Wang J*, et al.* Oxidative phosphorylation-dependent regulation of cancer cell apoptosis in response to anticancer agents. Cell Death &Amp; Disease **2015**;6:e1969
38. Venkatesh HS, Chaumeil MM, Ward CS, Haas-Kogan DA, James CD, Ronen SM. Reduced phosphocholine and hyperpolarized lactate provide magnetic resonance biomarkers of PI3K/Akt/mTOR inhibition in glioblastoma. Neuro Oncol **2012**;14:315-25
39. Silva MT. Secondary necrosis: the natural outcome of the complete apoptotic program. FEBS Lett **2010**;584:4491-9
40. Guerriero JL, Ditsworth D, Fan Y, Zhao F, Crawford HC, Zong W-X. Chemotherapy Induces Tumor Clearance Independent of Apoptosis. Cancer Research **2008**;68:9595-600
41. Witney TH, Kettunen MI, Brindle KM. Kinetic modeling of hyperpolarized 13C label exchange between pyruvate and lactate in tumor cells. J Biol Chem **2011**;286:24572-80
42. Keshari KR, Sriram R, Van Criekinge M, Wilson DM, Wang ZJ, Vigneron DB*, et al.* Metabolic reprogramming and validation of hyperpolarized 13C lactate as a prostate cancer biomarker using a human prostate tissue slice culture bioreactor. Prostate **2013**;73:1171-81
43. Hong R, Lim SC. (1)(8)F-fluoro-2-deoxyglucose uptake on PET CT and glucose transporter 1 expression in colorectal adenocarcinoma. World J Gastroenterol **2012**;18:168-74
44. Avril N. GLUT1 expression in tissue and (18)F-FDG uptake. J Nucl Med **2004**;45:930-2
45. Dong Y, Eskandari R, Ray C, Granlund KL, Santos-Cunha LD, Miloushev VZ*, et al.* Hyperpolarized MRI Visualizes Warburg Effects and Predicts Treatment Response to mTOR Inhibitors in Patient-Derived ccRCC Xenograft Models. Cancer Res **2019**;79:242-50
46. Elvas F, Boddaert J, Vangestel C, Pak K, Gray B, Kumar-Singh S*, et al.* (99m)Tc-Duramycin SPECT Imaging of Early Tumor Response to Targeted Therapy: A Comparison with (18)F-FDG PET. J Nucl Med **2017**;58:665-70
47. Balasubramanian Harisankar CN, Preethi R, John J. Metabolic flare phenomenon on 18 fluoride-fluorodeoxy glucose positron emission tomography-computed tomography scans in a patient with bilateral breast

cancer treated with second-line chemotherapy and bevacizumab. Indian J Nucl Med **2015**;30:145-7
48. Cassetta L, Noy R, Swierczak A, Sugano G, Smith H, Wiechmann L*, et al.* Isolation of Mouse and Human Tumor-Associated Macrophages. Adv Exp Med Biol **2016**;899:211-29
49. Kubota R, Yamada S, Kubota K, Ishiwata K, Tamahashi N, Ido T. Intratumoral distribution of fluorine-18-fluorodeoxyglucose in vivo: high accumulation in macrophages and granulation tissues studied by microautoradiography. J Nucl Med **1992**;33:1972-80
50. Liu X, Liu H, Yuan C, Zhang Y, Wang Y, Hu S*, et al.* CD68-positive tumor-associated macrophages predicts the survival of patients with stage I colorectal cancer. Int J Clin Exp Pathol **2016**;9:11676-81

Tables

	T_2 MRI	Bioluminescence	Fluorescence	[1-^{13}C]pyruvate MRSI	[^{18}F]FDG-PET			[^{18}F]FDG autoradiography	[^{18}F]FDG excised tumors	Histology	
Tumor type	**Volume (cm^3)**	**Mean Radiance ($p/s/cm^2/sr$)**	**Mean Radiant Efficiency ($[p/s/cm^2/sr] / [\mu W/cm^2]$)**	**Lactate/pyruvate ratio**	**SUV_{max}**	**SUV_{mean}**	**k_i (min^{-1})**	**Tumor/muscle ratio**	**%ID/g**	**CC3 (% positivity)**	**TUNEL (% positivity)**
Colo205											
Pre-treatment	0.879 ± 0.425 (n = 10)	$2.455 \times 10^9 \pm 3.445 \times 10^9$ (n = 10)	$1.465 \times 10^9 \pm 9.009 \times 10^8$ (n = 8)	2.525 ± 0.549 (n = 7)	2.103 ± 0.250 (n = 7)	1.131 ± 0.160 (n = 7)	0.048 ± 0.01 (n = 9)				
Post-treatment	0.829 ± 0.491 (n = 10)	$4.723 \times 10^8 \pm 5.678 \times 10^8$ ** (n = 10)	$2.068 \times 10^9 \pm 1.981 \times 10^9$ (n = 8)	1.414 ± 0.391 ** (n = 7)	2.134 ± 0.362 (n = 7)	1.087 ± 0.190 (n = 7)	0.037 ± 0.012 (n = 9)	4.096 ± 0.268 (n = 3)	7.613 ± 0.697 (n = 6)	58.510 ± 14.440 *** (n = 7)	19.360 ± 6.311 ** (n = 7)
Pre-control	0.705 ± 0.252 (n = 7)	$6.961 \times 10^8 \pm 9.705 \times 10^8$ (n = 8)	$1.373 \times 10^9 \pm 1.494 \times 10^9$ (n = 7)	1.975 ± 0.548 (n = 5)	2.261 ± 0.580 (n = 7)	1.230 ± 0.223 (n = 7)					
Post-control	0.721 ± 0.289 (n = 7)	$1.092 \times 10^9 \pm 1.406 \times 10^9$ (n = 8)	$1.288 \times 10^9 \pm 1.191 \times 10^9$ (n = 7)	2.106 ± 0.630 (n = 5)	2.219 ± 0.161 (n = 7)	1.182 ± 0.206 (n = 7)		4.011 ± 0.224 (n = 3)	8.846 ± 0.828 (n = 6)	21.800 ± 11.580 (n = 7)	8.005 ± 6.728 (n = 7)
MDA-MB-231											
Pre-treatment	0.939 ± 0.488 (n = 8)	$1.288 \times 10^9 \pm 4.629 \times 10^8$ (n = 12)	$3.002 \times 10^9 \pm 1.180 \times 10^9$ (n = 12)	2.236 ± 0.386 (n = 7)	2.219 ± 0.399 (n = 10)	1.045 ± 0.172 (n = 10)					
Post-treatment	0.862 ± 0.450 (n = 8)	$4.148 \times 10^8 \pm 4.340 \times 10^8$ **** (n = 12)	$1.634 \times 10^9 \pm 1.015 \times 10^9$ *** (n = 12)	1.382 ± 0.331 ** (n = 7)	1.977 ± 0.346 (n = 10)	0.877 ± 0.158 * (n = 10)				57.650 ± 19.300 ** (n = 5)	21.120 ± 6.061 ** (n = 5)
Pre-control	0.664 ± 0.281 (n = 9)	$1.541 \times 10^9 \pm 1.503 \times 10^9$ (n = 9)	$2.349 \times 10^9 \pm 1.067 \times 10^9$ (n = 9)	2.126 ± 0.588 (n = 9)	2.125 ± 0.558 (n = 9)	0.998 ± 0.214 (n = 9)					
Post-control	0.686 ± 0.304 (n = 9)	$1.067 \times 10^9 \pm 6.385 \times 10^8$ (n = 9)	$2.174 \times 10^9 \pm 1.110 \times 10^9$ (n = 9)	2.442 ± 0.607 (n = 9)	2.039 ± 0.685 (n = 9)	0.913 ± 0.275 (n = 9)				18.980 ± 5.092 (n = 4)	6.644 ± 1.944 (n = 4)

Table 1. Imaging, *ex vivo* and histological detection of treatment response 24 h after MEDI3039 treatment.

Figure legends

Figure 1. MEDI3039 treatment induces long-term regression of Colo205 tumors. (a-d) Tumor volumes (n=3) were determined by T_2-weighted MRI measurements. (e-h) mStrawberry fluorescence; (i-l) bioluminescence. The bioluminescence scale has been decreased by a factor of 10 for the images acquired on day 29.

Figure 2. Histological assessment of tumor cell death following treatment with MEDI3039. Tumor sections were stained for cleaved caspase 3 (CC3) and TUNEL (n = 7 per group, drug- and vehicle-treated). (a-c) CC3 and (g-i) TUNEL staining of Colo205 tumor sections taken 24 h after treatment of the animals with MEDI3039 (treatment) or drug vehicle (control). (d-f) CC3 and (j-l) TUNEL staining of MDA-MB-231 tumor sections taken 24 h after treatment of the animals with MEDI3039 (treatment) or drug vehicle (control).

Figure 3. Comparison of hyperpolarized [1-^{13}C]lactate/[1-^{13}C]pyruvate ratios and [^{18}F]FDG-PET SUV_{max} values in Colo205 and MDA-MB-231 tumors before and 24 h after treatment with MEDI3039. (a) A Colo205 tumor-bearing mouse before (top two rows of images) and after treatment (bottom two rows of images). Maximum intensity projections overlaid on bone reconstructions (top and bottom rows) and an axial slice through the tumor (middle two rows). The tumor is indicated by white arrows and a dashed outline. (b & d) [1-^{13}C]lactate/[1-^{13}C]pyruvate ratio before and after treatment in (b) Colo205 (n = 7 drug-treated and n = 5 vehicle-treated) and (d) MDA-MB-231 (n = 7 drug-treated and n = 9 vehicle-treated) tumors. (c & e) [^{18}F]FDG SUV_{max} before and after treatment in (c) Colo205 and (e) MDA-MB-231 tumors. Pre- and post-treatment images are identically scaled, PET images are scaled from an SUV of 0 – 1.5.

Figure 4. [^{18}F]FDG uptake in different cell populations in Colo205 tumors (n = 3 per group, drug- and vehicle-treated). Tumors were excised 24 h after treatment of the mice with MEDI3039 or drug vehicle (control). Disaggregated tumors were flow sorted and radioactivity in the different cell fractions was counted. Example sort profiles from (a) a control tumor and (b) a tumor treated with MEDI3039. (c) The percentage of different cell types in the tumors; (d) The percentage injected dose per cell for each cell type and (e) the percentage injected dose for each population of cells (i.e. the %ID per cell corrected for the percentage of each cell type) displayed as %ID per million sorted cells.

Figure 5. Changes in membrane transporter and enzyme expression and enzyme activity changes following treatment with MEDI3039. Arrows above the western blots indicate samples from post-treatment tumors. Expression of (a) MCT-1; (b) MCT-4; (c) LDH-A; (d) GLUT1; (e) GLUT3; (f) HK2; (g) PARP; and enzyme activity of (h) LDH; (i) GAPDH and (j) pyruvate kinase. Abbreviations: cPARP – cleaved PARP; uPARP – uncleaved PARP.

Figure 6. ^{13}C NMR measurements of Colo205 tumor extracts following [1,6 $^{13}C_2$]glucose infusions into tumor-bearing mice 24 h after drug vehicle (n = 3) or MEDI3039 (n = 3) treatment. Example ^{13}C NMR spectra from (a) a control tumor and (b) a treated tumor. Chemical shift assignments: 1, β-glucose C1; 2, α-glucose C1; 3,

β-glucose C6; 4, α-glucose C6; 5, lactate C3; 6, alanine C3. Insets: the spectra between 30 and 37 p.p.m. showing the difference in C3 and C4 glutamate labeling before treatment and after treatment. (c) Diagram showing the ^{13}C labeling pattern (blue) following [1,6 $^{13}C_2$]glucose infusion. (d) Comparison of ^{13}C labeled glucose and lactate concentrations in control and MEDI3039 treated tumors. Abbreviations: GLU – glutamate; S – singlet; D – doublet.

Figure 1

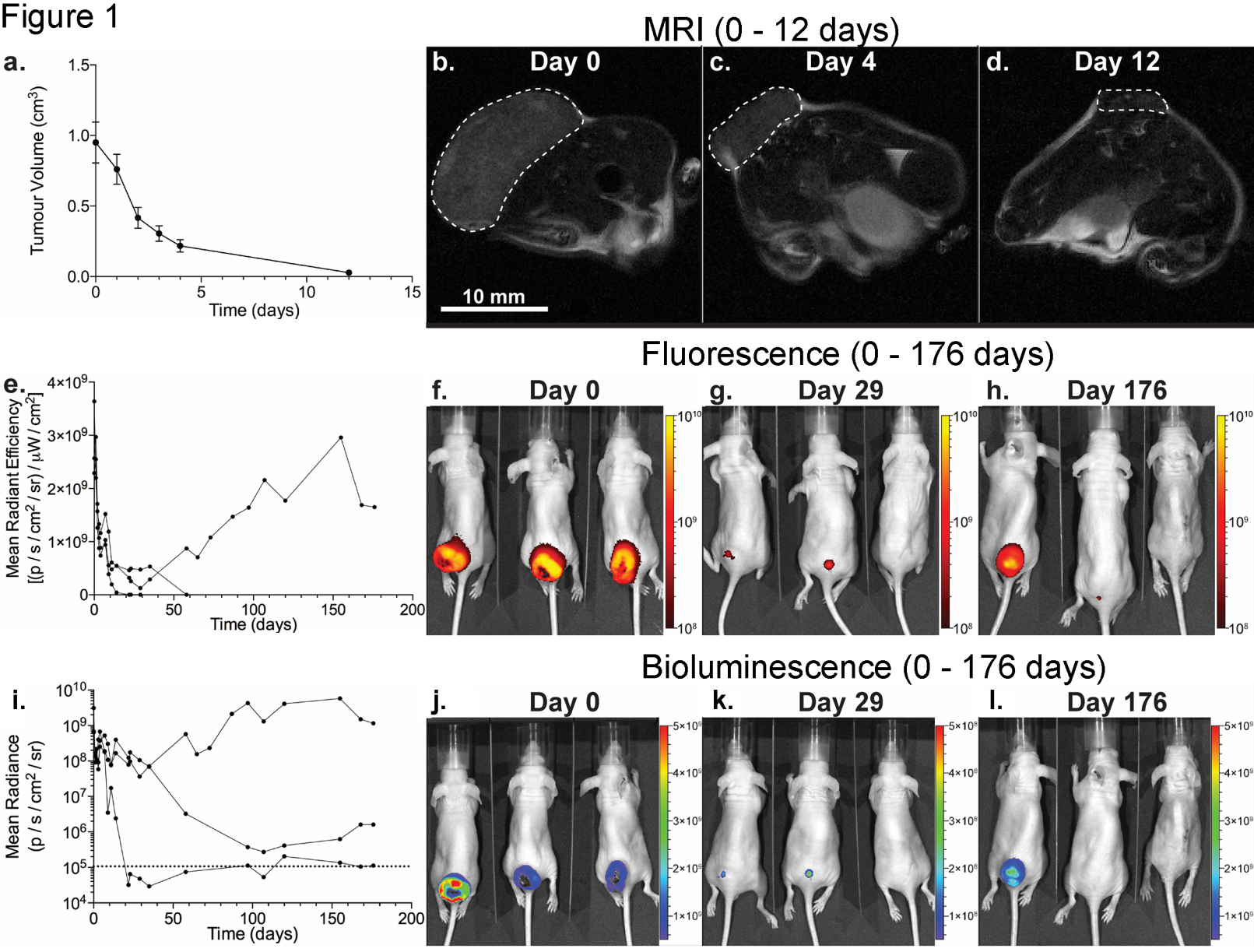
MRI (0 - 12 days)
a.
Tumour Volume (cm3)
Time (days)
b. Day 0
c. Day 4
d. Day 12
10 mm
Fluorescence (0 - 176 days)
e.
Mean Radiant Efficiency [(p / s / cm2 / sr) / µW / cm2]
Time (days)
f. Day 0
g. Day 29
h. Day 176
Bioluminescence (0 - 176 days)
i.
Mean Radiance (p / s / cm2 / sr)
Time (days)
j. Day 0
k. Day 29
l. Day 176

Figure 2

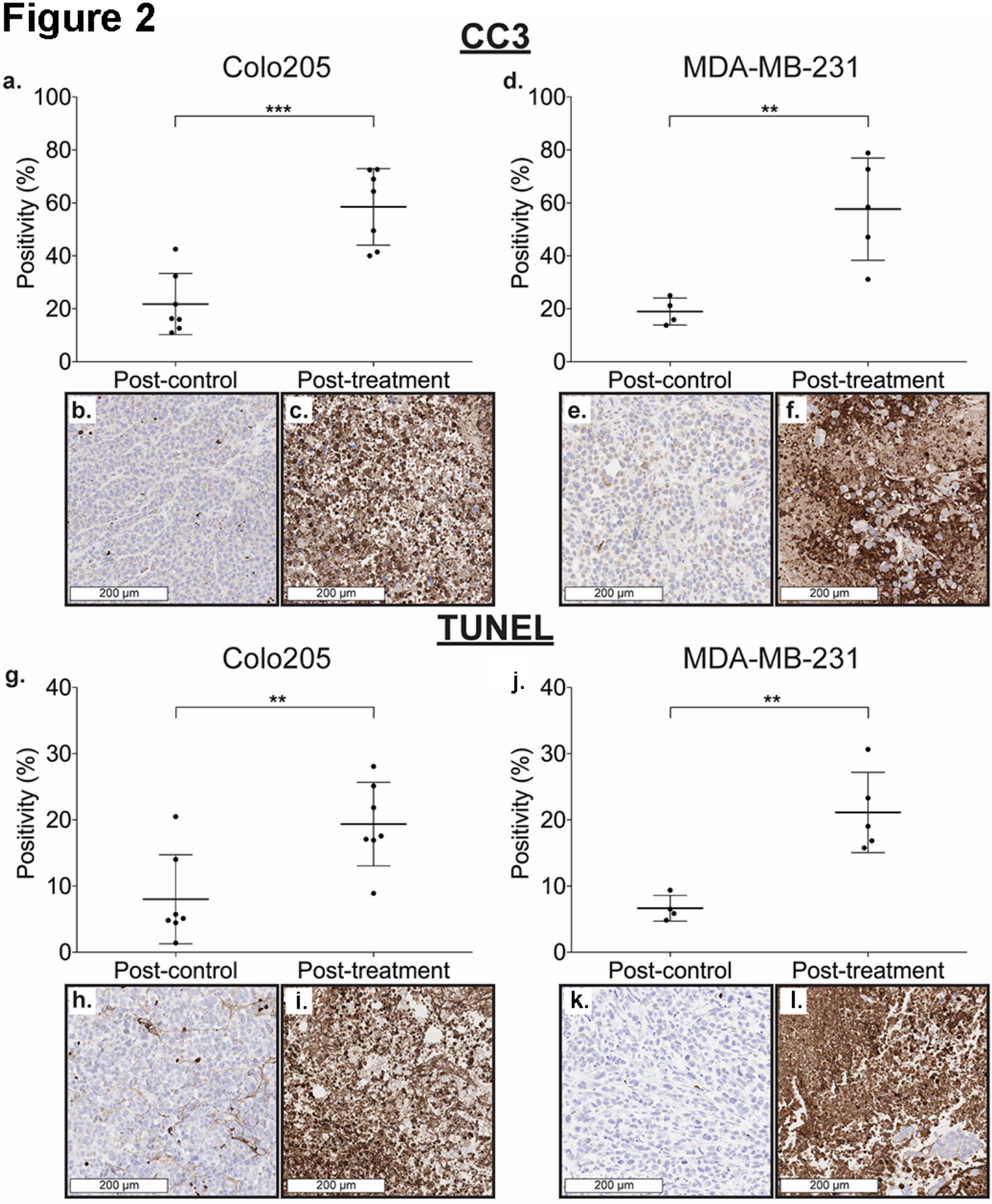
CC3
Colo205
a.
Positivity (%)
100
80
60
40
20
0
***
Post-control
Post-treatment
b.
c.
200 µm
200 µm
MDA-MB-231
d.
**
e.
f.
TUNEL
Colo205
g.
40
30
20
10
0
**
h.
i.
MDA-MB-231
j.
k.
l.

Figure 3

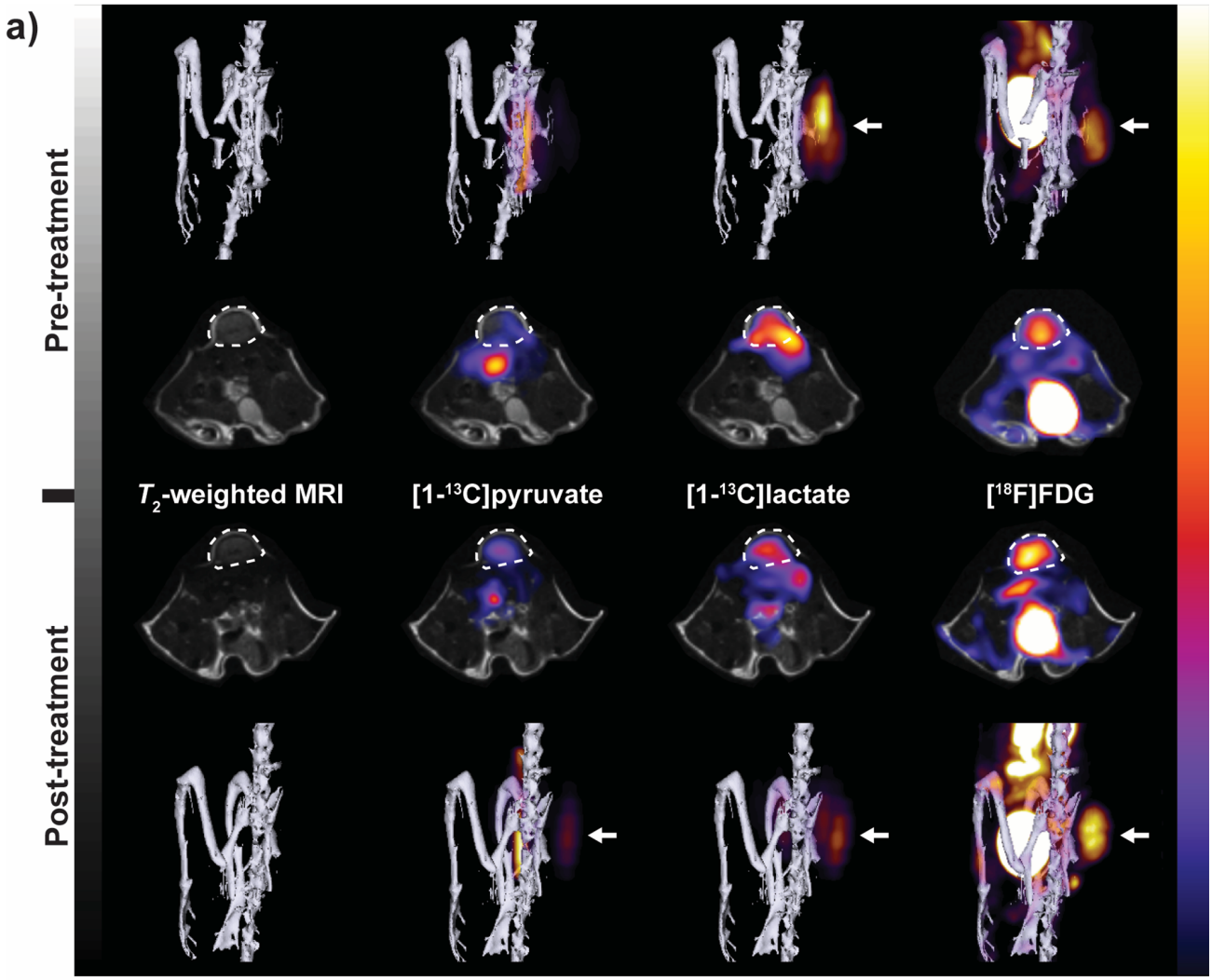

Colo205

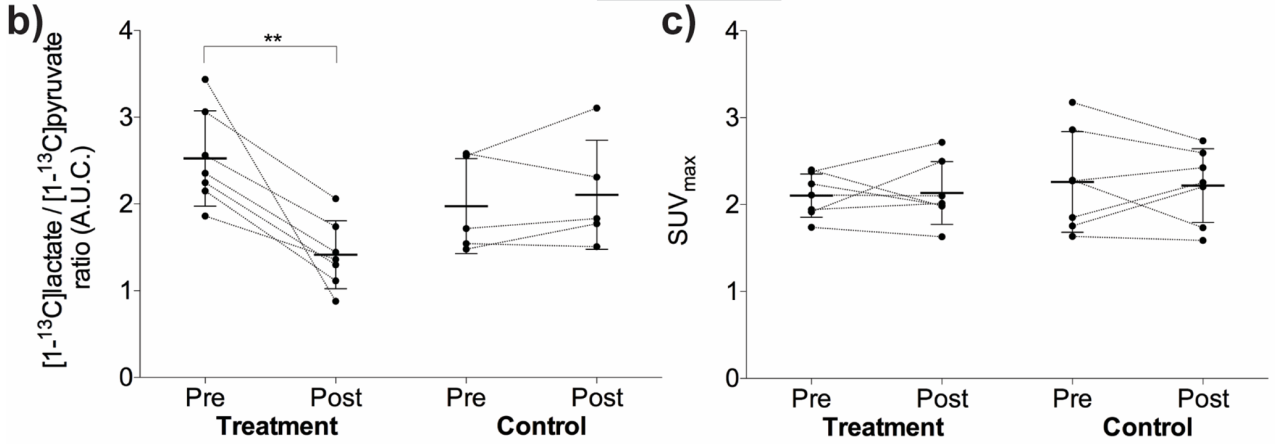

MDA-MB-231

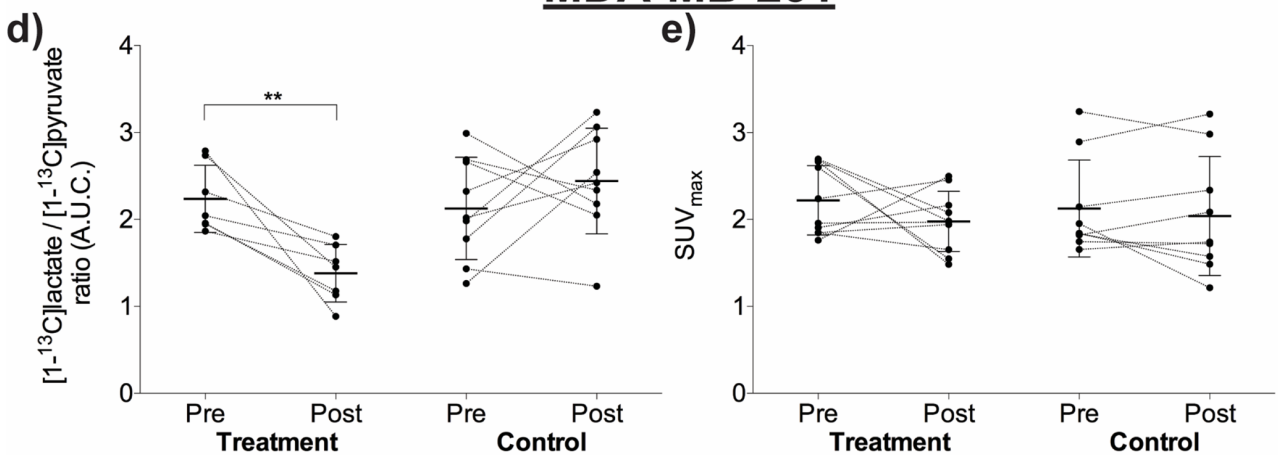

Figure 4

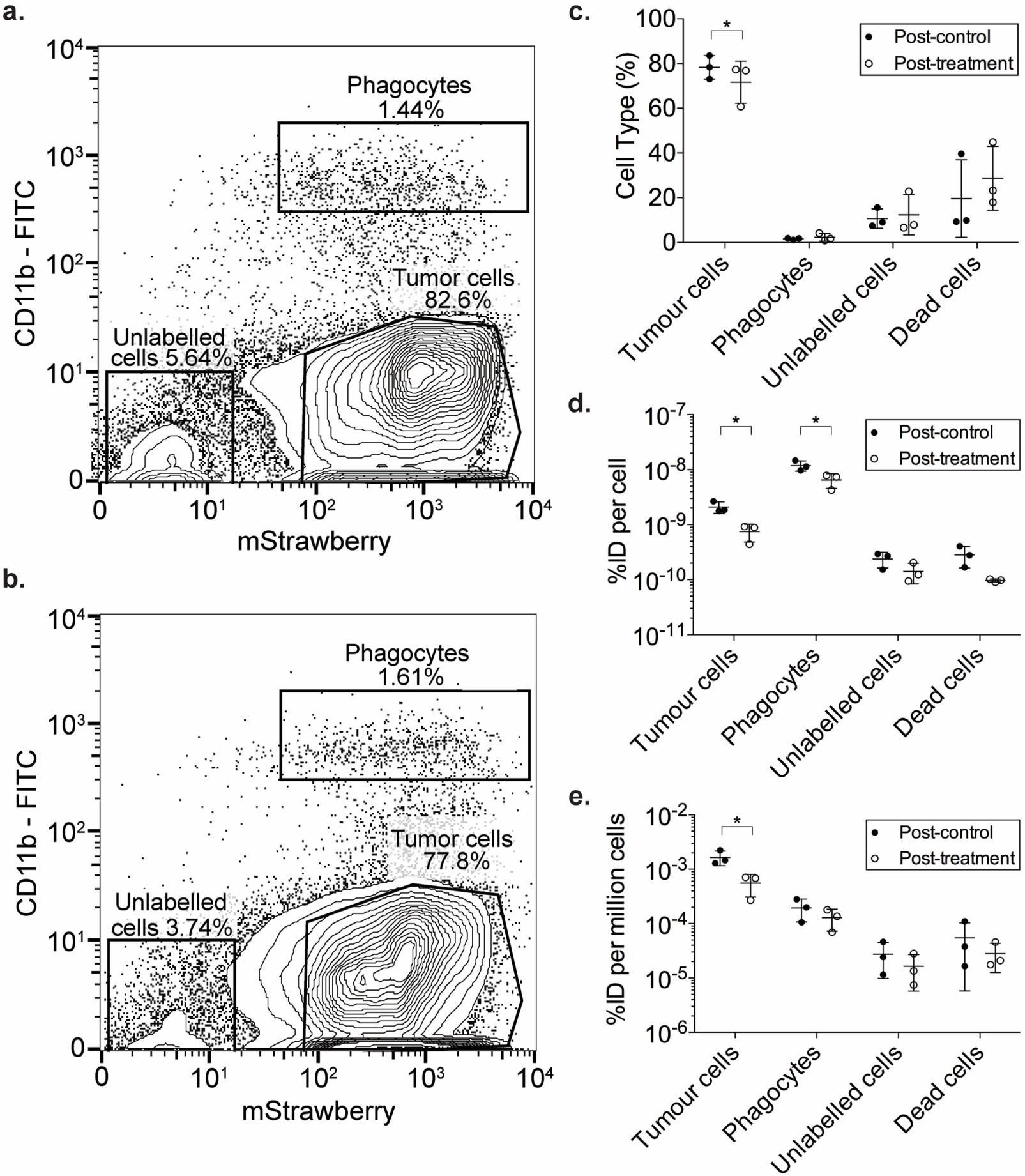
a.
Phagocytes
1.44%
Tumor cells
82.6%
Unlabelled
cells 5.64%
CD11b - FITC
mStrawberry
b.
Phagocytes
1.61%
Tumor cells
77.8%
Unlabelled
cells 3.74%
CD11b - FITC
mStrawberry
c.
Cell Type (%)
Post-control
Post-treatment
Tumour cells
Phagocytes
Unlabelled cells
Dead cells
d.
%ID per cell
Post-control
Post-treatment
Tumour cells
Phagocytes
Unlabelled cells
Dead cells
e.
%ID per million cells
Post-control
Post-treatment
Tumour cells
Phagocytes
Unlabelled cells
Dead cells

Figure 5

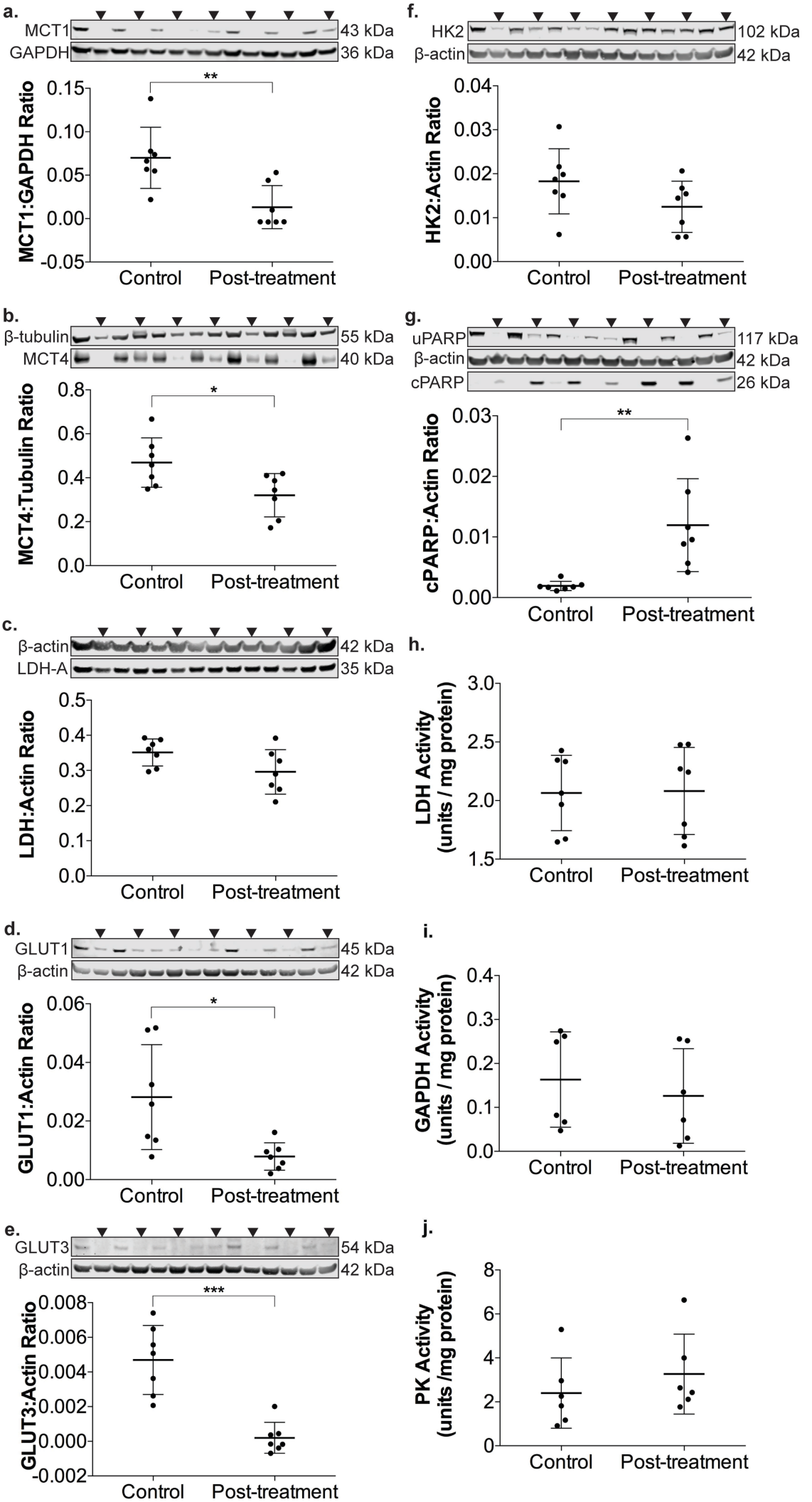
a.
MCT1
GAPDH
43 kDa
36 kDa
MCT1:GAPDH Ratio
0.15
0.10
0.05
0.00
-0.05
**
Control
Post-treatment
b.
β-tubulin
MCT4
55 kDa
40 kDa
MCT4:Tubulin Ratio
0.8
0.6
0.4
0.2
0.0
*
Control
Post-treatment
c.
β-actin
LDH-A
42 kDa
35 kDa
LDH:Actin Ratio
0.5
0.4
0.3
0.2
0.1
0.0
Control
Post-treatment
d.
GLUT1
β-actin
45 kDa
42 kDa
GLUT1:Actin Ratio
0.06
0.04
0.02
0.00
*
Control
Post-treatment
e.
GLUT3
β-actin
54 kDa
42 kDa
GLUT3:Actin Ratio
0.008
0.006
0.004
0.002
0.000
-0.002
***
Control
Post-treatment
f.
HK2
β-actin
102 kDa
42 kDa
HK2:Actin Ratio
0.04
0.03
0.02
0.01
0.00
Control
Post-treatment
g.
uPARP
β-actin
cPARP
117 kDa
42 kDa
26 kDa
cPARP:Actin Ratio
0.03
0.02
0.01
0.00
**
Control
Post-treatment
h.
LDH Activity
(units / mg protein)
3.0
2.5
2.0
1.5
Control
Post-treatment
i.
GAPDH Activity
(units / mg protein)
0.4
0.3
0.2
0.1
0.0
Control
Post-treatment
j.
PK Activity
(units /mg protein)
8
6
4
2
0
Control
Post-treatment

Figure 6

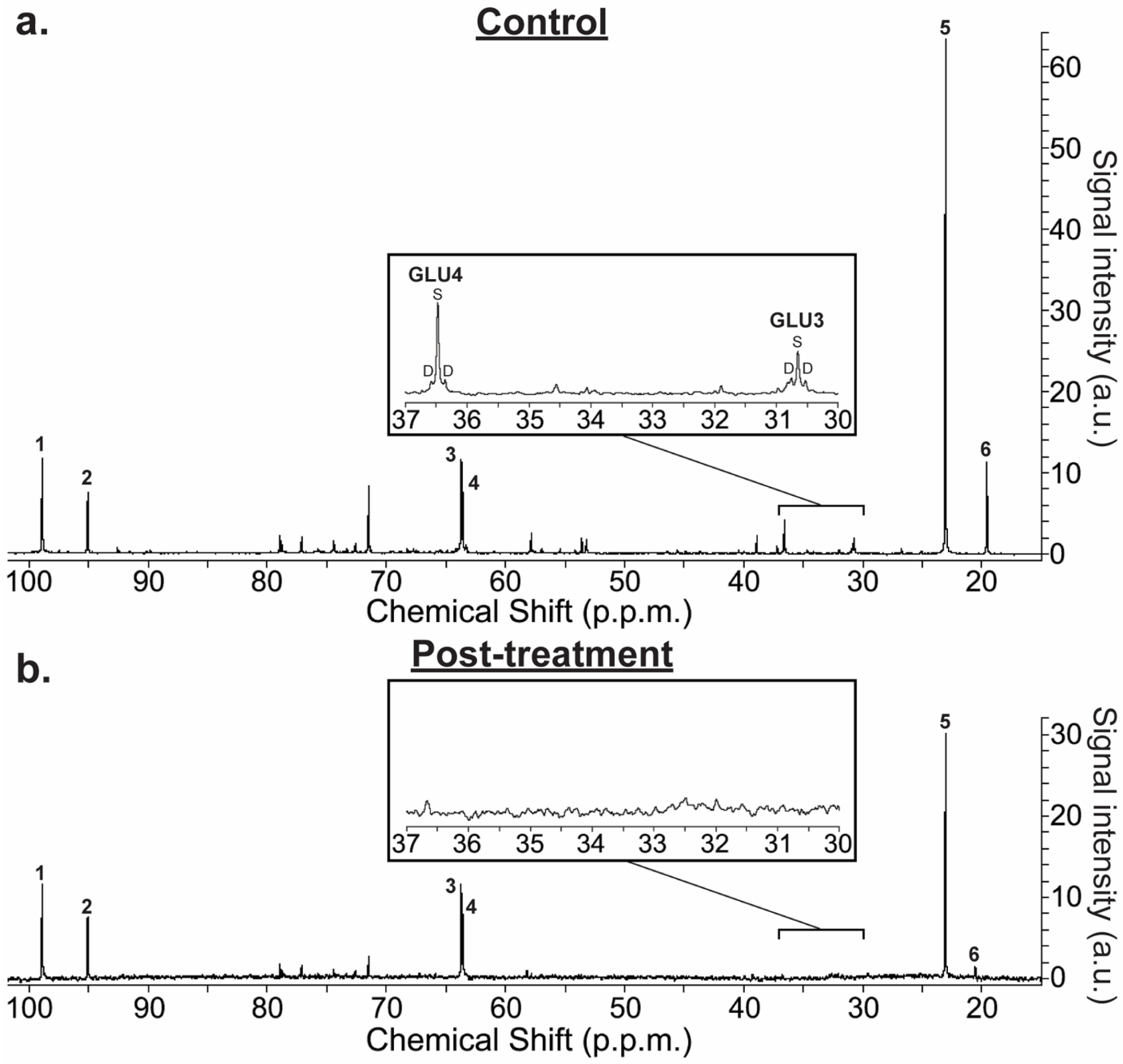
a.
Control
GLU4
S
D D
GLU3
S
D D
37 36 35 34 33 32 31 30
1
2
3
4
5
6
100 90 80 70 60 50 40 30 20
Chemical Shift (p.p.m.)
Signal intensity (a.u.)
0 10 20 30 40 50 60
b.
Post-treatment
37 36 35 34 33 32 31 30
1
2
3
4
5
6
100 90 80 70 60 50 40 30 20
Chemical Shift (p.p.m.)
Signal intensity (a.u.)
0 10 20 30

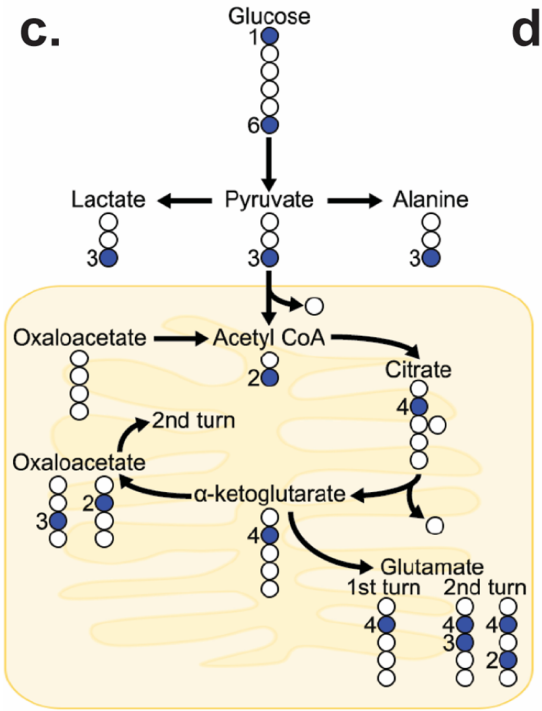
c.
Glucose
1
6
Lactate
Pyruvate
Alanine
3
3
3
Oxaloacetate
Acetyl CoA
2
Citrate
4
2nd turn
Oxaloacetate
3
2
α-ketoglutarate
4
Glutamate
1st turn
2nd turn
4
4
3
4
2

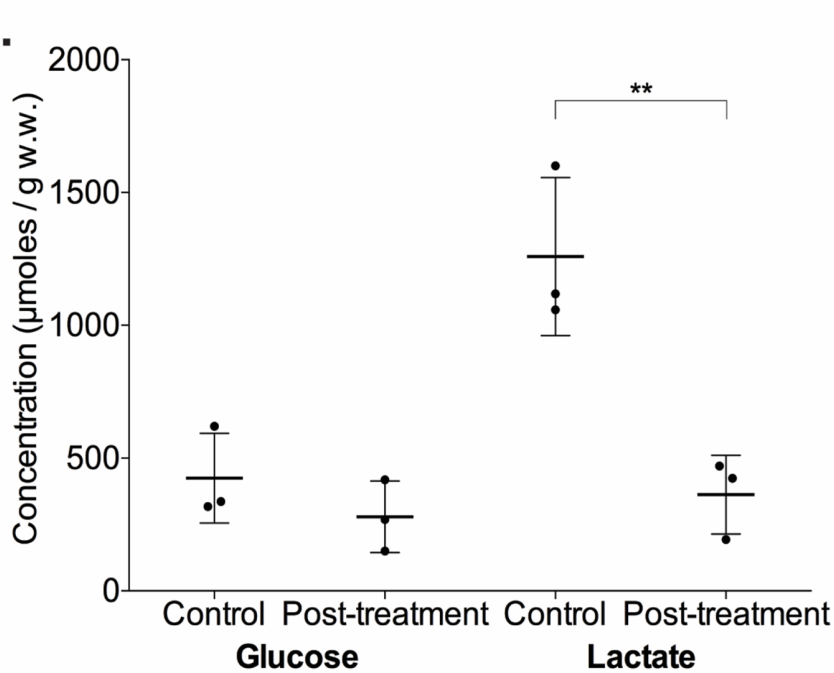
d.
Concentration (µmoles / g w.w.)
0 500 1000 1500 2000
**
Control
Post-treatment
Control
Post-treatment
Glucose
Lactate